Geophysical Research Letters

RESEARCH LETTER
10.1029/2020GL087499

Two Layers of Melting Ice Particles Within a Single Radar Bright Band: Interpretation and Implications

Haoran Li[1] and **Dmitri Moisseev**[1,2]

[1]Institute for Atmospheric and Earth System Research/Physics, Faculty of Science, University of Helsinki, Helsinki, Finland, [2]Finnish Meteorological Institute, Helsinki, Finland

Key Points:

- Two-layer LDR signature is observed by vertically pointing W- and C-band radars in a melting layer of precipitation
- Doppler spectra reveal that these layers are caused by the melting of needles, potentially generated by rime-splintering, and background ice
- The melting signal of small needles is used to evaluate current methods for the identification of melting layer boundaries

Correspondence to:
H. Li,
haoran.li@helsinki.fi

Citation:
Li, H., & Moisseev, D. (2020). Two layers of melting ice particles within a single radar bright band: Interpretation and implications. *Geophysical Research Letters*, *47*, e2020GL087499. https://doi.org/10.1029/2020GL087499

Received 12 FEB 2020
Accepted 4 JUN 2020
Accepted article online 9 JUN 2020

Abstract Dual-frequency dual-polarization radar observations of the melting of two ice populations in a stratiform rainfall event are presented. The observed phenomenon occurs as a two-layer linear depolarization ratio (LDR) signature in a single radar bright band. Doppler spectra observations show that the upper LDR layer is caused by the melting of ice needles, potentially generated by the rime-splintering process, while the lower one is mainly due to the melting of background ice particles formed at the cloud top. The melting signal of small needles acts as a unique benchmark for detecting the onset of melting and is used to verify the current methods for the identification of melting layer boundaries. The radar-derived characteristics of the melting layer are found to be dependent on the radar variable and frequency used. The implications of the presented findings for radar-based studies of precipitation properties in and above the melting layer are also discussed.

Plain Language Summary The melting layer of precipitation is a relatively narrow layer where snowflakes melt into raindrops. This layer is clearly visible in weather radar observations and is often called the " bright band" because of the stronger radar return coming from this region. In this paper, we present an event where two layers of melting ice particles, as indicated by dual-polarization radar observations, are present inside one bright band. Using state-of-the-art radar observations, we show that this phenomenon is caused by the melting of two ice particle populations. The upper layer is due to the melting of ice needles that are potentially generated by the rime-splintering process, and the second layer is caused by snowflakes that have formed at the cloud top. The measurements presented illustrate the complexity of ice clouds, where several populations of ice particles might coexist and evolve. We show how the multifrequency radar observations that are currently becoming more and more prevalent can be used to get a glimpse into the precipitation processes taking place in and above the melting layer. We also discuss how currently used methods to describe melting layer properties may be biased depending on what radar observations are used.

1. Introduction

The majority of rainfall in middle to high latitudes over land originates from ice clouds (Field & Heymsfield, 2015; Mülmenstädt et al., 2015). The region where snowflakes melt into raindrops typically occupies a relatively narrow layer, namely, the melting layer (ML), in stratiform precipitation (Fabry & Zawadzki, 1995). It is, nonetheless, important for precipitation development. Through latent heat exchange it can influence the dynamics of precipitation systems (Stewart et al., 1984; Szeto et al., 1988) and the local ambient environment (Carlin & Ryzhkov, 2019). On the other hand, it has been found that the macroscale properties of the ML are modulated by precipitation microphysical processes taking place inside (Heymsfield et al., 2015) and above the ML (e.g., Fabry & Zawadzki, 1995; Kumjian et al., 2016; Wolfensberger et al., 2016). Even though detailed observations of the ML are performed using aircraft penetrations, they are limited to measurement campaigns and do not provide continuous records. Ground-based radars have been widely employed for ML studies (e.g., Fabry & Zawadzki, 1995; Griffin et al., 2020; Kumjian et al., 2016; Li et al., 2020; Russchenberg & Ligthart, 1996; Trömel et al., 2019). However, radar interpretations of the ML are still challenging largely due to the uncertainties in microphysical processes that take place in the ML (Heymsfield et al., 2015) and how snowflake melting modifies particle physical (Leinonen & von Lerber, 2018) and scattering properties (Ori & Kneifel, 2018).

The manifestation of the ML in traditional cm-wavelength weather radar observations is a layer of enhanced radar reflectivity, which is often referred to as the bright band. In stratiform precipitation, the bright band is an excellent indicator of the ML (Fabry & Zawadzki, 1995). This distinct feature has been utilized in detecting the ML boundaries and inferring cloud microphysical properties above (Zawadzki et al., 2005). On the other hand, if not taken into account, it can bias the radar-based quantitative precipitation estimation (Fabry et al., 1992; Smyth & Illingworth, 1998). The rapid increase of the dielectric properties of snowflakes due to melting also leads to some unique characteristics of dual-polarization radar measurements in the ML, such as the significant dip in the co-polar correlation coefficient ρ_{hv} (e.g., Giangrande et al., 2008; Matrosov et al., 2007; Ryzhkov & Zrnic, 1998; Wolfensberger et al., 2016; Zrnic et al., 1993), increased values of differential reflectivity Z_{dr} (e.g., Hall et al., 1984; Kumjian et al., 2016; Ryzhkov & Zrnic, 1998; Zrnic et al., 1993), and linear depolarization ratio (LDR, e.g., Dias Neto et al., 2019; Le & Chandrasekar, 2012; Smyth & Illingworth, 1998). Those polarimetric observations show reasonably good agreement with radar reflectivity (Brandes & Ikeda, 2004) and have been applied to identify the ML for radars (e.g., Dias Neto et al., 2019; Giangrande et al., 2008; Kumjian et al., 2016; Wolfensberger et al., 2016). Numerical simulations have indicated that the backscattering properties of melting ice particles are affected by radar frequencies (Tyynelä et al., 2014), while there seems to be a lack of comparisons of those polarimetric observations at different radar bands.

Our interpretation of the ML signatures is often based on the assumption of one population of ice particles undergoing transformation due to the melting. Therefore, the radar signatures observed have been used to infer changes in the particle properties, such as shape, size, and melting fraction of the single particle population (e.g., Carlin & Ryzhkov, 2019; Russchenberg & Ligthart, 1996; von Lerber et al., 2014). A number of studies have reported the coexistence of multiple populations of ice particles, for example, as observed in Doppler radar spectra (Moisseev et al., 2015; Oue et al., 2015; Spek et al., 2008; Verlinde et al., 2013; Zawadzki et al., 2001). To our knowledge, there are no reports on how multiple ice particle populations modify the properties of the ML. This is important given that more and more efforts being devoted to developing sophisticated models that attempt to explain dual-polarization and multifrequency radar observations of the ML and how it is impacted by ice microphysics (Carlin & Ryzhkov, 2019; Johnson et al., 2016; Ori & Kneifel, 2018; Russchenberg & Ligthart, 1996; Tyynelä et al., 2014). Additionally, a seemingly trivial question on how to identify the onset of melting in radar observations is not completely resolved (Wolfensberger et al., 2016). In this study, we present observations of two populations of ice particles undergoing melting, using multifrequency dual-polarization Doppler radar observations. Furthermore, we show how different estimators of the ML boundaries perform and find that some of them are biased by as much as 100 m.

2. Data

The University of Helsinki Station for Measuring Ecosystem-Atmosphere Relation II (SMEAR II) is located in Hyytiälä, Southern Finland (61.845°N, 24.287°E, 150 m above mean sea level). The SMEAR II station hosts extensive instrumentation for measuring biosphere-atmosphere interactions, which include cloud and precipitation sensors. In this study, two vertically pointing radars located at the station are used. These observations are supplemented by the National Centers for Environmental Prediction (NCEP) reanalysis data set to provide information on the atmospheric state.

2.1. C- and W-Band Radars

Since 2016, a vertically pointing C-band dual-polarization Doppler radar (HYytiälä Doppler RAdar, HYDRA-C) (Moisseev et al., 2015) has been deployed at the station. In November 2017, the radar measurement setup was extended by the installation of a 94-GHz dual-polarization frequency-modulated continuous-wave Doppler cloud radar (HYDRA-W) (Küchler et al., 2017). In addition to reflectivity, LDR, Doppler velocity, and spectrum width, which are observed by both radars, HYDRA-W records Doppler spectra. HYDRA-C operates with a maximum unambiguous Doppler velocity of 4.98 m s^{-1}. The settings of HYDRA-W observations depend on the range. Below 996 m, range resolution is 25.5 m and Doppler spectra are computed using a 1,024-point fast Fourier transform (FFT) with Nyquist velocity of 10.24 m s^{-1}. For heights between 996 and 3,577 m, range resolution is kept the same, while the Doppler spectrum is computed using a 512-point FFT with Nyquist velocity of 5.12 m s^{-1}. As part of spectral processing, the noise power is estimated for each range gate. Spectral lines that have powers within five standard deviations

from the estimated noise power are rejected. For heights above 3,577 m, range resolution is decreased to 34 m, while the Doppler measurements are performed using the same settings. The temporal resolutions of HYDRA-C and HYDRA-W measurements are 1.37 and 3.35 s, respectively.

2.2. NCEP Data Set

The NCEP reanalysis data sets with the grid spacing of 52.6 km are used to derive temperature profiles over the Hyytiälä station. The wet-bulb temperature is computed based on the predicted air temperature and relative humidity (Stull, 2011). The time resolution of the NCEP data sets is 3 hr. The height resolution is around 0.2 km below 1 km and about 0.5 km between 1 and 4 km. The NCEP data are linearly interpolated into the time and range resolutions of HYDRA-W.

3. Observations

3.1. Measurements of Radar Moments

3.1.1. Overview of This Event

During 18–19 April 2018, a stratiform rainfall system with the melting level of around 1.2 km above ground passed over the Hyytiälä station. According to NCEP, the wind direction changed from westerly to northerly during this event. From 21:00 UTC to 24:00 UTC on 18 April 2014, the wind between 1 and 2.5 km was more or less northwesterly with the speeds between 6 and 8 m s^{-1}. As shown in Figure 1, the depth of the precipitating system extended to 4–5 km where the cloud top temperature was −20°C to −15°C. The C-band radar reflectivity observations show a distinct bright band signature, which descended from ∼1.2 km to ∼0.9 km during the event. At W-band, the bright band was not as pronounced, because of non-Rayleigh scattering effects (Heymsfield et al., 2008; Kollias & Albrecht, 2005) and attenuation in rain and the ML (Li & Moisseev, 2019).

3.1.2. Two-Layer LDR Signature

If we zoom in and study the ML signatures between 21:20 and 22:35 UTC, as presented in Figure 2, we will see that for about 30 min starting from 21:20 UTC, two distinct LDR layers can be observed. The area presented in Figure 2 is shown by the black rectangle in the Figure 1. These two layers, while clearly visible in the LDR observations, cannot be identified in the reflectivity and velocity observations at either frequency. This signature is more pronounced in the W-band measurements because of their higher vertical resolution. Previous studies have reported observations of double MLs, which were attributed to temperature inversion (Ikeda et al., 2005). However, neither NCEP data nor the closest radiosonde observations show any evidence of a temperature inversion at this height.

Above the two-layer LDR region, an area of relatively high LDR values is present. In this area, which extends to altitudes of around 2.2 km, ice particles exhibit LDR values as large as −16 dB. The air temperature at the top of this high LDR region is roughly −6°C. Wolde and Vali (2001) have proposed that such high LDR values in ice can be attributed either to columnar ice crystals or graupel. Oue et al. (2015) have shown that the LDR signal around −15 dB in snow can be attributed to needle-like particles based on scattering calculations and observations. The increase of Doppler velocity at both C- and W-bands around the radar bright band indicates the transition from snowflakes to raindrops.

At the later stages of this period, the precipitation intensifies and both radars (Figures $2a_2$ and $2b_2$) show a commonly observed single-LDR-layer in the ML. The C-band LDR observations show a slightly descending trend as can be identified between 21:50 and 22:35 UTC. The local sagging of C-band LDR in the ML (Kumjian et al., 2016) coincides with two fall streaks at around 22:25 UTC and 22:35 UTC, which can be explained by the locally enhanced aggregation and precipitation rate (Carlin & Ryzhkov, 2019; Li et al., 2020). In contrast, W-band LDR shows less variation in the ML at these times. Smaller particles are usually lighter than larger ones. After the onset of melting, the liquid volume fraction in smaller particles increases faster than in larger particles, resulting in a faster increase in the refractive index of small particles (Bringi & Chandrasekar, 2001). Therefore, W-band LDR, which is more sensitive to smaller particles, increases more rapidly than C-band LDR. In addition, small particles fall more slowly than the larger ones and travel less distance within a given time. As a result, the altitude where the LDR significantly increases is higher at the W-band.

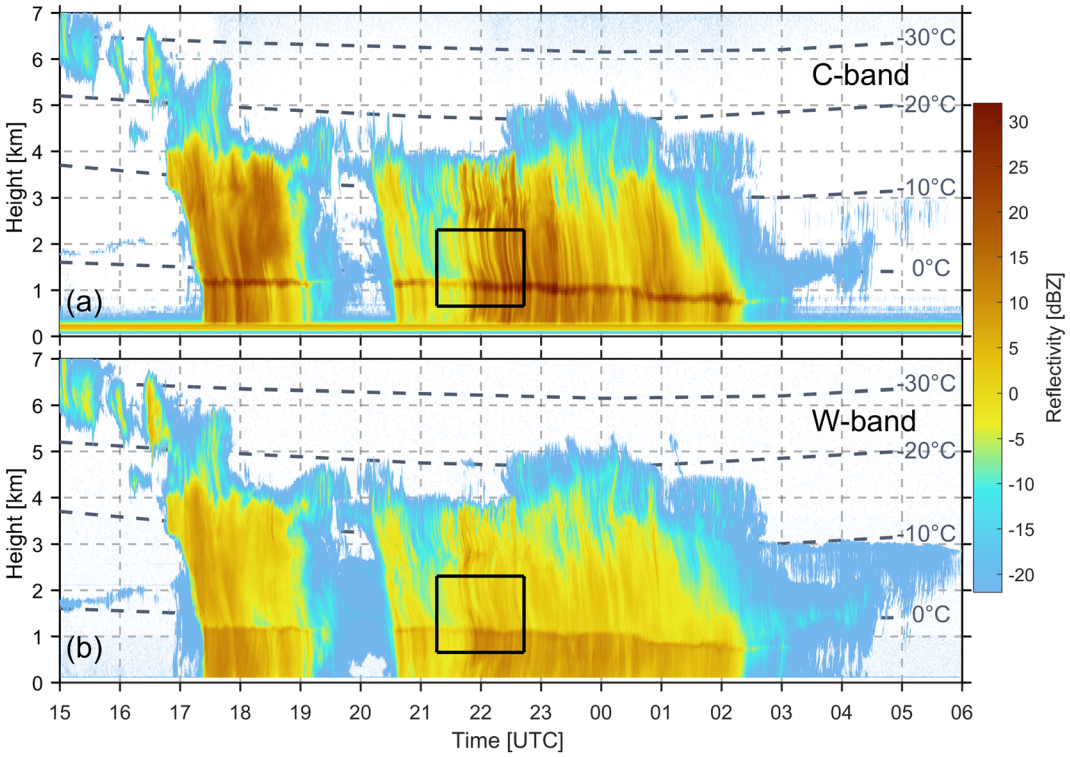

Figure 1. HYDRA-C (a) and HYDRA-W (b) observations from 18 April 2014 15:00 to 19 April 2014 06:00 UTC. Gray dashed lines indicate isothermal layers of −30°C, −20°C, −10°C, and 0°C. High-resolution views of the observations in black boxes are shown in Figure 2.

3.2. Precipitation Analysis Along Fall Streaks

Changes in the growth conditions of ice particles often lead to the formation of fall streaks that can be observed in radar measurements (Marshall, 1953; Pfitzenmaier et al., 2017), as can be seen in Figure 2a$_1$. If the vertical wind direction and/or speed change, the fall streaks deviate from the vertical (Lauri et al., 2012), as is the case during this event. The resulting slanted trails of ice particles can make the ML boundaries indistinguishable if the reflectivity profiles at vertical incidence are used (Fabry & Zawadzki, 1995). Therefore, to investigate the origins of the two-layer LDR signature, analysis is performed along particle trails as identified using the radar signatures of fall streaks. To this end, we have identified three trails that are marked as A, B, and C in Figure 2a$_1$. These trails were selected to study not only the origin of these two-layer signatures but also the transition from two-layer to single-layer LDR.

The trails were identified by tracing the locally enhanced C-band reflectivity observations (Fabry & Zawadzki, 1995). Because reflectivity measurements at the dual-LDR-layer region do not exhibit clear fall streaks, observations at 21:55 UTC were used instead. The identified trail is marked by the dashed line in Figure 2a$_1$. Then, the dashed line was shifted to the time of interest, around 21:45 UTC, as shown by the solid line A. Visual analysis of the shifted trail and the reflectivity field showed good agreement. Furthermore, there were no significant changes in the wind field during these 10 min. Hence, the shifted trail is a good fall-streak approximation for this period. Similarly, Trails B and C (solid lines) were traced to study the transition from the two-layer to the single-layer LDR region. Since the wind shear may have changed a little during this event, shifting the dashed line to Location A may not be perfect. But this approach presents a much better view of the falling paths of hydrometeors (Fabry & Zawadzki, 1995). Real-time trail tracing could have been possible if the horizontal wind observations had been available (Lauri et al., 2012; Pfitzenmaier et al., 2017).

3.2.1. Trail A in the Two-Layer LDR Region

To investigate the origin of the phenomenon observed, Doppler spectra analysis was performed. The W-band cloud radar records both co-polar and cross-polar Doppler spectra, from which Doppler power and LDR spectra can be computed. The dual-polarization radar spectra can be used to identify and classify multiple

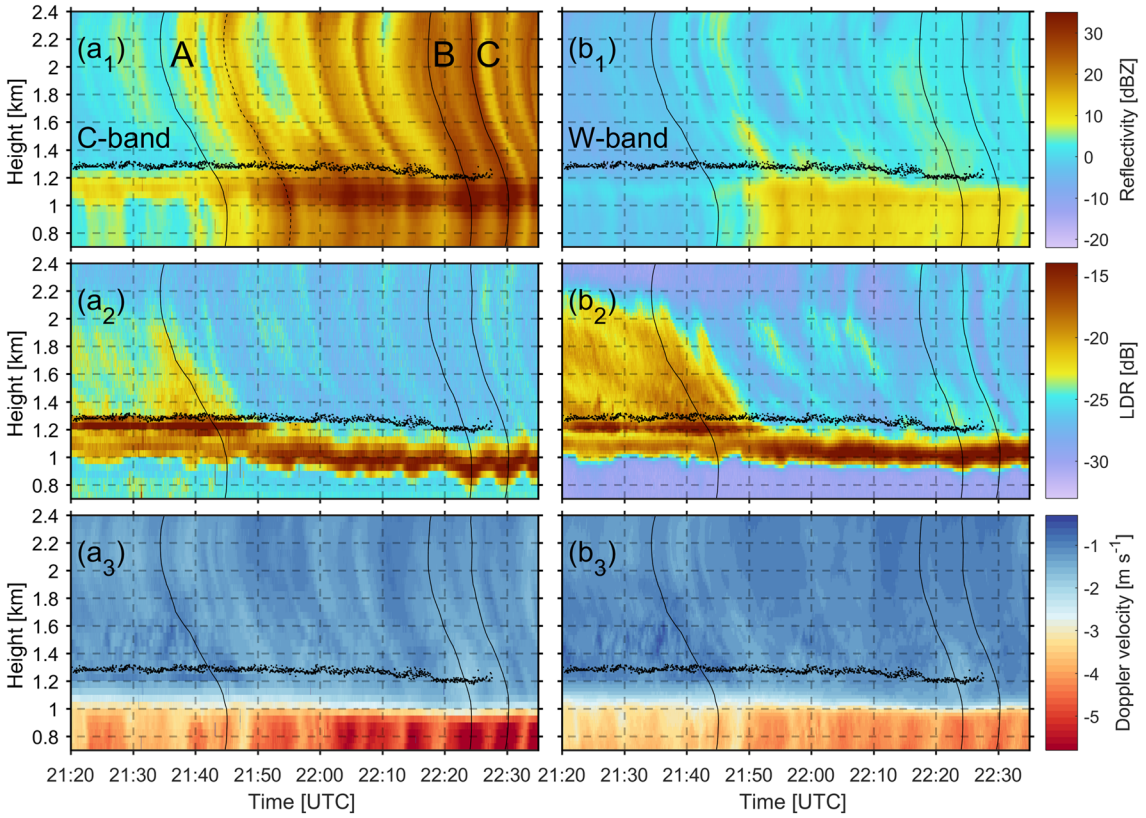

Figure 2. Radar reflectivity, LDR, and Doppler velocity observed by HYDRA-C ($a_{1,2,3}$) and HYDRA-W ($b_{1,2,3}$) from 18 April 2014 21:20 to 22:35 UTC. The black dashed line and solid lines B and C in panel (a_1) indicate fall streaks traced using the local maxima of the C-band radar reflectivity. Trail A is obtained by shifting the dashed line. Dots around 1.2 km indicate the derived melting layer top by using needle-LDR as discussed in section 3.2.1.

populations of hydrometers (Oue et al., 2015; Spek et al., 2008). Therefore, in addition to reflectivity and LDR profiles computed along the trails, power and LDR spectra were also calculated. These observations are shown in Figure 3. The observed reflectivity (blue) and LDR (orange) at C- and W-bands for Trail A are shown in Figure 3a_1. Two layers of enhanced LDR at both bands are present, while only one bright band can be identified from C-band radar reflectivity observations. The profiles of LDR at both frequencies in the ML match fairly well. The first LDR peak at both bands reaches −13 dB at 1.2 km, followed by another weaker and lower one (about −18 dB) collocated with the peak of C-band radar reflectivity. As expected, W-band reflectivity does not exhibit the bright band feature. Then the LDR values at both radar bands decrease toward the lowest level which conventionally marks the bottom of the ML (Dias Neto et al., 2019; Le & Chandrasekar, 2012; Sandford et al., 2017) where raindrops are much more symmetric and the cross-polar radar signal depends mainly on the cross-coupling between the polarization channels (Moisseev et al., 2002).

The Doppler power spectra observed by HYDRA-W show the presence of two populations of ice particles, as can be seen in Figure 3a_2. The slower falling particles, with the mean Doppler velocity under 1 m s^{-1}, are generated at altitudes around 2.3 km where the temperature is just below −5°C, and there is a clearly identifiable supercooled liquid water mode in the Doppler spectrum at around 0 m s^{-1} (Kalesse et al., 2019) with background ice falling from above. The spectral LDR observations for these particles show relatively large values of about −15 dB. This enhanced-LDR area has Doppler velocities close to 0 m s^{-1}, ruling out the possibility that these ice particles are aggregates or graupel. Oue et al. (2015) have reported very similar spectra observations within the columnar-ice-crystal-growth temperature regime in snowfall and classified those slow-falling ice crystals as needles. This conclusion supports our observations that these slow-falling particles are newly formed needles generated in the region favorable for Hallett-Massop secondary ice production (Hallett & Mossop, 1974). This inference is also in agreement with single-scattering studies (Aydin & Walsh, 1999; Tyynelä et al., 2011).

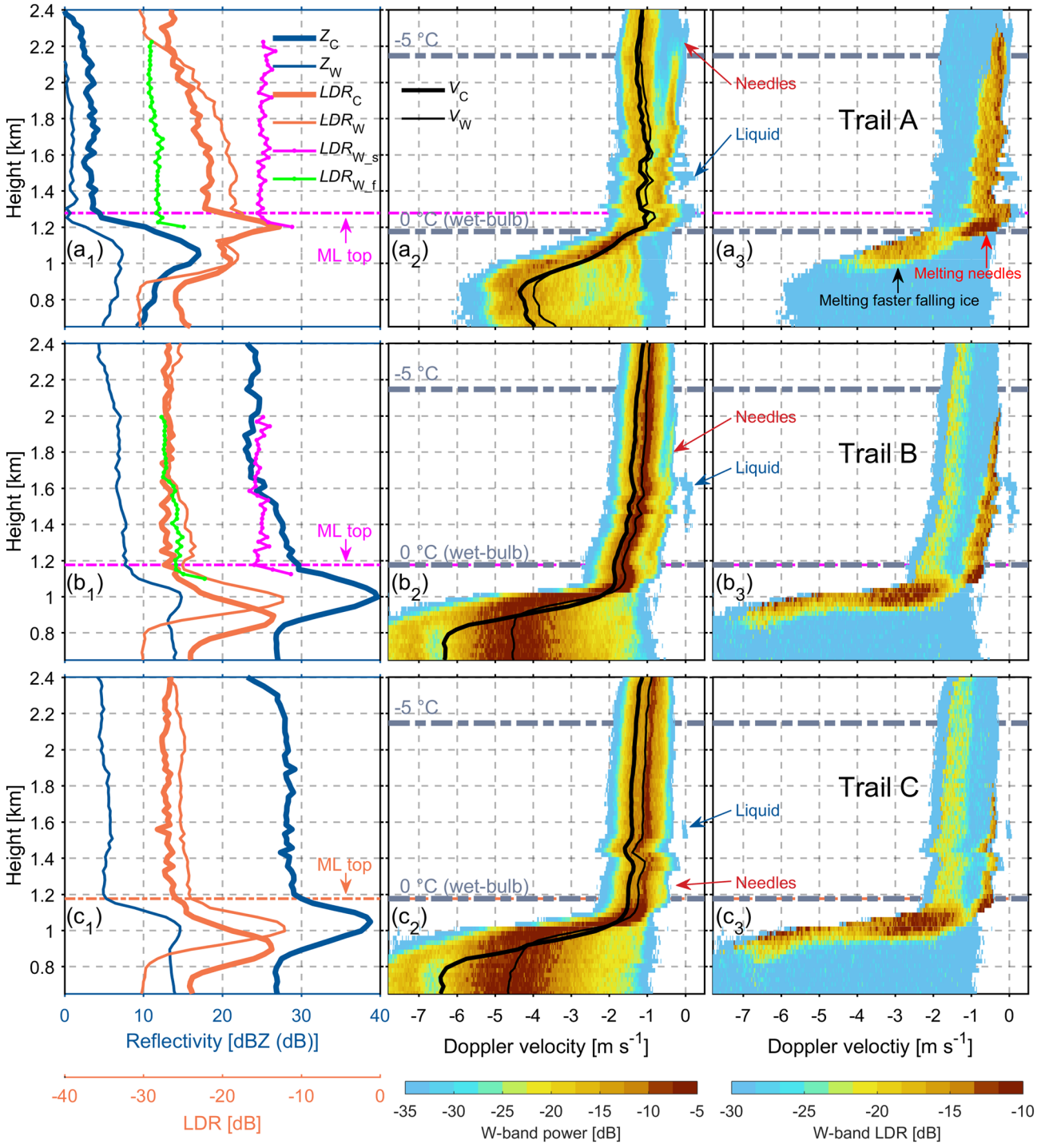

Figure 3. Observed reflectivity and LDR at C- and W-bands for Trails A (a_1), B (b_1), and C (c_1). Vertical profiles of Doppler power spectra (a_2, b_2, and c_2) and LDR (a_3, b_3, and c_3) for Trails A, B, and C recorded by HYDRA-W. Purple and green lines indicate LDR of slower falling needles (LDR_{W_s}) and faster falling background ice (LDR_{W_f}), respectively, in panels (a_1) and (b_1). Purple dashed lines in panels (a_1) and (b_1) indicate melting layer (ML) tops derived from needle-LDR. In panel (c_1), the ML top (orange dashed line) is derived based on W-band LDR since the needle signal is barely detectable in the Doppler spectrum. Black thick and thin lines indicate Doppler velocities measured by HYDRA-C and HYDRA-W, respectively. Gray thick dashed lines in panels ($a_{2,3}$), ($b_{2,3}$), and ($c_{2,3}$) indicate the air temperature of −5°C and the wet-bulb temperature of 0°C, respectively. Negative Doppler velocity indicates downward motion. The unit of spectral power (reflectivity) is $mm^6\,m^{-3}\,(m\,s^{-1})^{-1}$. Since there is no accepted nomenclature for denoting the spectral power (reflectivity) in the dB scale, we simply use dB here.

The faster falling particles are produced at the cloud top, 4–5 km above the ground. The Doppler velocities of these particle vary between 1 and 2 m s^{-1}. Their LDR values do not exceed −25 dB. We cannot provide an exact classification of these particles, since these observations can be caused by either aggregates, lightly rimed aggregates, or densely rimed crystals. However, the exact classification of ice particles is not critical in this study. We need only point out that we have two populations of ice crystals, one that is faster falling and another slower. The faster falling particles have larger masses, while the slower falling crystals, which are most probably needles, are lighter.

Because of the differences in fall velocities and masses, melting would affect the radar variables of ice needles before those of faster falling particles. The melting process increases the refractive index of ice particles, more quickly for smaller needles, and therefore enhances dual-polarization radar signatures, such as LDR (Bringi & Chandrasekar, 2001). Therefore, it is expected that the LDR of needles will increase first. This can be observed in Figure $3a_3$. The W-band spectral LDR of the slower falling particles starts to increase at the height of 1.28 km while the LDR values of the faster falling particles begin to grow about 50 m lower. According to these observations, melting ends at about 1.1 km for the needles and around 0.9 km for the faster ice particles. This difference in the melting explains why two LDR layers are observed inside a single ML.

To study this effect in more detail, two populations of ice particles were separated based on a well-defined dip in spectral power. Similar to Oue et al. (2015), the LDR of slower falling ice (LDR_{W_s}) is the ratio of the integrated power spectrum at H and V channels and expressed on the dB scale. The LDR of faster falling ice (LDR_{W_f}) is derived in the same way. In Figure $3a_1$, vertical profiles of LDR_{W_s} and LDR_{W_f} are shown and compared to the bulk reflectivity and LDR as measured by both radars. Additionally, LDR_{W_s} is used to identify the ML top, which is defined as the height where the slope of the LDR profile changes (Brandes & Ikeda, 2004). This was done for the rest of the event, where needle signatures could be clearly identified in the spectra observations. The results are shown in Figure 2 by black dots.

The ML top, as detected using radar needle observations, is about 100 m above 0°C (wet-bulb), which is within the model errors (Mittermaier & Illingworth, 2003). The mean Doppler velocity, which is often used as an indicator of melting (Hogan & O'Connor, 2004; Illingworth et al., 2007), starts increasing around 100 m below the detected ML top. This is not surprising. The increase in fall velocity occurs at the more advanced melting stages, where the melt fraction of ice particles typically exceeds 10–20% (Mitra et al., 1990). While the LDR of faster falling particles reacts later to melting, the C-band reflectivity starts to increase at about the same height as LDR_{W_s}. This possibly indicates that radar reflectivity may be a reliable measure for the detection of the ML top, as also discussed by Wolfensberger et al. (2016).

3.2.2. Trails B and C in the One-Layer LDR Region

By studying the evolution of the precipitation system, as shown in Figure 2, one can see that the precipitation intensifies after 21:50 UTC and the LDR values in the ice part of the precipitation decrease at the same time. This indicates that the relative contribution of needles to the radar observations decreases. Similarly, the two-layer LDR signature disappears. However, spectral measurements still show detectable needle mode and therefore the LDR of needles can be retrieved and the ML top estimated. After about 22:25 UTC, the needle signal in the Doppler spectra fades and can no longer be used reliably.

The computed Doppler spectra and profiles of the radar variable along Trails B and C are shown in Figures 3b and 3c. As can be seen, while the needle spectral mode is still detectable in Trail B, it has merged with the spectrum of the background ice in Trail C. Compared to Trail A, Trail B and Trail C observations show the presence of larger ice particles, that is, higher fall velocities in rain, a spectral dip between 6 and 7 m s^{-1} due to the resonance scattering of raindrops with a diameter of ∼1.7 mm (Kollias et al., 2002). The C- and W- band reflectivity-weighted Doppler velocities (Figures $3b_2$ and $3c_2$) are different for these two trails, which is attributed to the increased importance of non-Rayleigh scattering at least for the W-band observations.

The comparison of vertical profiles of LDR measured by C- and W-band radars shows that the relative positions of LDR peaks have shifted from one another. The W-band LDR is higher by about 100 m. Changes in slope of the LDR profiles (which we call "break points") can be used to identify the ML top and bottom. Similar to the locations of the LDR peaks, these breakpoints in the C-band and W-band LDR profiles are shifted relative to each other. Interestingly, the profile of the C-band reflectivity follows the W-band LDR more closely than the C-band LDR. For Trail B, the needle LDR can still be estimated from W-band

spectra. The ML top estimated from this profile seems close to the one computed from the bulk W-band LDR (not shown). For Trail C, we cannot perform this retrieval due to the weak needle mode in W-band spectra. But the ML top computed from W-band LDR matches rather well with the height where the spectral LDR of needles starts to increase, as shown in Figure $3c_3$. These observations demonstrate that the ML top computed from W-band LDR or C-band reflectivity observations are closer to the actual height where melting starts. The C-band LDR observations tend to underestimate the height of the ML top.

The observations around the ML bottom parts show a different story though. The break point of LDR and reflectivity should indicate the height where larger particles complete their melting. However, the break point of the C-band LDR profile is lower than those of C-band reflectivity and W-band LDR. The W-band spectral LDR observations do not show what causes such a difference. Unfortunately, HYDRA-C did not record spectra for this event, and we cannot check if there were high C-band spectral LDR values in the spectrum after the W-band LDR reached the break point. Nonetheless, even though we cannot pinpoint the cause of the difference, we conclude that C-band LDR observations would give the height where most, if not all, melting completes. Therefore, the C-band reflectivity and W-band LDR would overestimate the height of the ML bottom.

4. Summary and Conclusions

On 18 April 2018, a stratiform rainfall system moved over the University of Helsinki SMEAR II station in Hyytiälä, Finland. The vertically pointing C- and W-band radars recorded two layers of enhanced LDR inside a single radar bright band. These two layers were caused by the melting of two populations of ice particles, namely, ice needles, generated in the region favorable to Hallett-Massop secondary ice production, and background ice formed at the cloud top. While the two-layer LDR signature was clearly visible for 30 min, the Doppler spectra observations exhibited the presence of two populations of ice particles for about an hour.

The observations show that multiple populations of ice particles may become visible in the dual-polarization radar observations of the precipitation ML. Given that the coexistence of multiple ice populations has been reported over various geographical areas, for example, the Arctic (Oue et al., 2015), North America (Korolev et al., 2020; Zawadzki et al., 2001), the United Kingdom (Hogan et al., 2002; Keppas et al., 2017), and China (Yang et al., 2014), more reports of this phenomenon are expected in the future. The distinctive polarimetric signals of small needles can be employed to determine the height of the top of the ML. Even though the measurements presented are from vertically pointing radars, it is expected that similar features should also be visible in scanning weather radar observations, for example, Z_{dr}, LDR, and ρ_{hv}.

The multifrequency dual-polarization radar measurements presented show that ML characteristics, as identified from radar observations, depend on what radar frequency and variable are used. This dependency arises from the sensitivity of radar observations at different frequencies to particles of different sizes, which in their turn have different melting properties. Because needles have small masses and terminal velocities, their properties are changed very quickly by melting. This provides an excellent benchmark for the detection of the top of the ML. Our analysis shows that the ML top is best identified by the change of slopes in bulk W-band LDR or C-band reflectivity observations. The similarity between the W-band LDR and C-band reflectivity profiles in the ML is somewhat surprising and requires further study. If the ML top is derived from C-band LDR or mean Doppler velocity, its height may be underestimated by as much as 100 m.

The bottom of the ML appears to be better represented by the C-band LDR observations, which show enhanced values after C-band reflectivity and W-band LDR values have decreased to the levels observed in rain. The analysis of the W-band Doppler power and LDR spectra could not explain what causes these larger C-band LDR values. Future studies that use both C- and W-band spectral observations are needed to investigate the later stages of melting.

Overall, we show that radar-observed characteristics of the ML are sensitive to ice particle microphysical properties. Therefore, dual-polarization radar variables and their spectra, observed at different frequencies, carry complimentary information, which can be used to advance our understanding of the precipitation processes taking place in and above the ML.

Data Availability Statement

The presented HYDRA-W and HYDRA-C data are available at https://doi.org/10.5281/zenodo.3661127.

Acknowledgments
Matti Leskinen and Jussi Tiira are acknowledged for their help in data analysis. We are grateful to two anonymous referees for their constructive feedback. The research of Haoran Li and Dmitri Moisseev was supported by Academy of Finland (Grant 305175) and the Academy of Finland Finnish Center of Excellence program (Grant 307331). Haoran Li was also funded by China Scholarship Council. We are in preparation for releasing long-term radar measurements in the Hyytiälä station.

References

Aydin, K., & Walsh, T. M. (1999). Millimeter wave scattering from spatial and planar bullet rosettes. *IEEE Transactions on Geoscience and Remote Sensing*, *37*(2), 1138–1150.

Brandes, E. A., & Ikeda, K. (2004). Freezing-level estimation with polarimetric radar. *Journal of Applied Meteorology*, *43*(11), 1541–1553.

Bringi, V. N., & Chandrasekar, V. (2001). *Polarimetric Doppler weather radar*. Cambridge: Cambridge University Press.

Carlin, J. T., & Ryzhkov, A. V. (2019). Estimation of melting layer cooling rate from dual-polarization radar: Spectral bin model simulations. *Journal of Applied Meteorology and Climatology*, *58*(7), 1485–1508.

Dias Neto, J., Kneifel, S., Ori, D., Trömel, S., Handwerker, J., Bohn, B., et al. (2019). The TRIple-frequency and Polarimetric radar Experiment for improving process observations of winter precipitation. *Earth System Science Data*, *11*(2), 845–863.

Fabry, F., Austin, G. L., & Tees, D. (1992). The accuracy of rainfall estimates by radar as a function of range. *Quarterly Journal of the Royal Meteorological Society*, *118*(505), 435–453.

Fabry, F., & Zawadzki, I. (1995). Long-term radar observations of the melting layer of precipitation and their interpretation. *Journal of the Atmospheric Sciences*, *52*(7), 838–851.

Field, P. R., & Heymsfield, A. J. (2015). Importance of snow to global precipitation. *Geophysical Research Letters*, *42*, 9512–9520. https://doi.org/10.1002/2015GL065497

Giangrande, S. E., Krause, J. M., & Ryzhkov, A. V. (2008). Automatic designation of the melting layer with a polarimetric prototype of the WSR-88D radar. *Journal of Applied Meteorology and Climatology*, *47*(5), 1354–1364.

Griffin, E. M., Schuur, T. J., & Ryzhkov, A. V. (2020). A polarimetric radar analysis of ice microphysical processes in melting layers of winter storms using s-band quasi-vertical profiles. *Journal of Applied Meteorology and Climatology*, *59*(4), 751–767. https://doi.org/10.1175/JAMC-D-19-0128.1

Hall, M. P. M., Goddard, J. W. F., & Cherry, S. M. (1984). Identification of hydrometeors and other targets by dual-polarization radar. *Radio Science*, *19*(1), 132–140.

Hallett, J., & Mossop, S. C. (1974). Production of secondary ice particles during the riming process. *Nature*, *249*(5452), 26.

Heymsfield, A. J., Bansemer, A., Matrosov, S., & Tian, L. (2008). The 94-GHz radar dim band: Relevance to ice cloud properties and CloudSat. *Geophysical Research Letters*, *35*, L03802. https://doi.org/10.1029/2007GL031361

Heymsfield, A. J., Bansemer, A., Poellot, M. R., & Wood, N. (2015). Observations of ice microphysics through the melting layer. *Journal of the Atmospheric Sciences*, *72*(8), 2902–2928.

Hogan, R. J., Field, P. R., Illingworth, A. J., Cotton, R. J., & Choularton, T. W. (2002). Properties of embedded convection in warm-frontal mixed-phase cloud from aircraft and polarimetric radar. *Quarterly Journal of the Royal Meteorological Society*, *128*(580), 451–476.

Hogan, R. J., & O'Connor, E. J. (2004). *Facilitating cloud radar and lidar algorithms: The Cloudnet instrument synergy/target categorization product*. UK: University of Reading. Retrieved from http://www.met.rdg.ac.uk/~swrhgnrj/publications/categorization.pdf

Ikeda, K., Brandes, E. A., & Rasmussen, R. M. (2005). Notes and correspondence: Polarimetric radar observation of multiple freezing levels. *Journal of the Atmospheric Sciences*, *62*(10), 3624–3636.

Illingworth, A. J., Hogan, R. J., O'Connor, E. J., Bouniol, D., Brooks, M. E., Delanoé, J., et al. (2007). Cloudnet. *Bulletin of the American Meteorological Society*, *88*(6), 883–898. https://doi.org/10.1175/bams-88-6-883

Johnson, B. T., Olson, W. S., & Skofronick-Jackson, G. (2016). The microwave properties of simulated melting precipitation particles: Sensitivity to initial melting. *Atmospheric Measurement Techniques*, *9*, 9–21.

Küchler, N., Kneifel, S., Löhnert, U., Kollias, P., Czekala, H., & Rose, T. (2017). A W-band radar-radiometer system for accurate and continuous monitoring of clouds and precipitation. *Journal of Atmospheric and Oceanic Technology*, *34*(11), 2375–2392.

Kalesse, H., Vogl, T., Paduraru, C., & Luke, E. (2019). Development and validation of a supervised machine learning radar doppler spectra peak-finding algorithm. *Atmospheric Measurement Techniques*, *12*(8), 4591–4617.

Keppas, S. C., Crosier, J., Choularton, T. W., & Bower, K. N. (2017). Ice lollies: An ice particle generated in supercooled conveyor belts. *Geophysical Research Letters*, *44*, 5222–5230. https://doi.org/10.1002/2017GL073441

Kollias, P., & Albrecht, B. (2005). Why the melting layer radar reflectivity is not bright at 94 GHz. *Geophysical Research Letters*, *32*, L24818. https://doi.org/10.1029/2005GL024074

Kollias, P., Albrecht, B. A., & Marks, F. Jr. (2002). Why Mie? Accurate observations of vertical air velocities and raindrops using a cloud radar. *Bulletin of the American Meteorological Society*, *83*(10), 1471–1484.

Korolev, A., Heckman, I., Wolde, M., Ackerman, A. S., Fridlind, A. M., Ladino, L. A., et al. (2020). A new look at the environmental conditions favorable to secondary ice production. *Atmospheric Chemistry and Physics*, *20*(3), 1391–1429.

Kumjian, M. R., Mishra, S., Giangrande, S. E., Toto, T., Ryzhkov, A. V., & Bansemer, A. (2016). Polarimetric radar and aircraft observations of saggy bright bands during MC3E. *Journal of Geophysical Research: Atmospheres*, *121*, 3584–3607. https://doi.org/10.1002/2015JD024446

Lauri, T., Koistinen, J., & Moisseev, D. (2012). Advection-based adjustment of radar measurements. *Monthly Weather Review*, *140*(3), 1014–1022.

Le, M., & Chandrasekar, V. (2012). Hydrometeor profile characterization method for dual-frequency precipitation radar onboard the GPM. *IEEE Transactions on Geoscience and Remote Sensing*, *51*(6), 3648–3658.

Leinonen, J., & von Lerber, A. (2018). Snowflake melting simulation using smoothed particle hydrodynamics. *Journal of Geophysical Research: Atmospheres*, *123*, 1811–1825. https://doi.org/10.1002/2017JD027909

Li, H., & Moisseev, D. (2019). Melting layer attenuation at Ka- and W-bands as derived from multifrequency radar Doppler spectra observations. *Journal of Geophysical Research: Atmospheres*, *124*, 9520–9533. https://doi.org/10.1029/2019JD030316

Li, H., Tiira, J., von Lerber, A., & Moisseev, D. (2020). Towards the connection between snow microphysics and melting layer: Insights from multi-frequency and dual-polarization radar observations during BAECC. *Atmospheric Chemistry and Physics Discussions*, *2020*, 1–23. https://doi.org/10.5194/acp-2020-16

Mülmenstädt, J., Sourdeval, O., Delanoë, J., & Quaas, J. (2015). Frequency of occurrence of rain from liquid-, mixed-, and ice-phase clouds derived from A-Train satellite retrievals. *Geophysical Research Letters*, *42*, 6502–6509. https://doi.org/10.1002/2015GL064604

Marshall, J. S. (1953). Precipitation trajectories and patterns. *Journal of Meteorology*, *10*(1), 25–29.

Matrosov, S. Y., Clark, K. A., & Kingsmill, D. E. (2007). A polarimetric radar approach to identify rain, melting-layer, and snow regions for applying corrections to vertical profiles of reflectivity. *Journal of Applied Meteorology and Climatology*, *46*(2), 154–166.

Mitra, S. K., Vohl, O., Ahr, M., & Pruppacher, H. R. (1990). A wind tunnel and theoretical study of the melting behavior of atmospheric ice particles. IV: Experiment and theory for snow flakes. *Journal of the Atmospheric Sciences*, *47*(5), 584–591.

Mittermaier, M. P., & Illingworth, A. J. (2003). Comparison of model-derived and radar-observed freezing-level heights: Implications for vertical reflectivity profile-correction schemes. *Quarterly Journal of the Royal Meteorological Society*, *129*(587), 83–95.

Moisseev, D. N., Lautaportti, S., Tyynela, J., & Lim, S. (2015). Dual-polarization radar signatures in snowstorms: Role of snowflake aggregation. *Journal of Geophysical Research: Atmospheres*, *120*, 12,644–12,655. https://doi.org/10.1002/2015JD023884

Moisseev, D. N., Unal, C. M. H., Russchenberg, H. W. J., & Ligthart, L. P. (2002). Improved polarimetric calibration for atmospheric radars. *Journal of Atmospheric and Oceanic Technology*, *19*(12), 1968–1977.

Ori, D., & Kneifel, S. (2018). Assessing the uncertainties of the discrete dipole approximation in case of melting ice particles. *Journal of Quantitative Spectroscopy and Radiative Transfer*, *217*, 396–406.

Oue, M., Kumjian, M. R., Lu, Y., Verlinde, J., Aydin, K., & Clothiaux, E. E. (2015). Linear depolarization ratios of columnar ice crystals in a deep precipitating system over the arctic observed by zenith-pointing Ka-band Doppler radar. *Journal of Applied Meteorology and Climatology*, *54*(5), 1060–1068.

Pfitzenmaier, L., Dufournet, Y., Unal, C. M. H., & Russchenberg, H. W. J. (2017). Retrieving fall streaks within cloud systems using Doppler radar. *Journal of Atmospheric and Oceanic Technology*, *34*(4), 905–920.

Russchenberg, H. W. J., & Ligthart, L. P. (1996). Backscattering by and propagation through the melting layer of precipitation: A new polarimetric model. *IEEE Transactions on Geoscience and Remote sensing*, *34*(1), 3–14.

Ryzhkov, A. V., & Zrnic, D. S. (1998). Discrimination between rain and snow with a polarimetric radar. *Journal of Applied Meteorology*, *37*(10), 1228–1240.

Sandford, C., Illingworth, A., & Thompson, R. (2017). The potential use of the linear depolarization ratio to distinguish between convective and stratiform rainfall to improve radar rain-rate estimates. *Journal of Applied Meteorology and Climatology*, *56*(11), 2927–2940.

Smyth, T. J., & Illingworth, A. J. (1998). Radar estimates of rainfall rates at the ground in bright band and non-bright band events. *Quarterly Journal of the Royal Meteorological Society*, *124*(551), 2417–2434.

Spek, A. L. J., Unal, C. M. H., Moisseev, D. N., Russchenberg, H. W. J., Chandrasekar, V., & Dufournet, Y. (2008). A new technique to categorize and retrieve the microphysical properties of ice particles above the melting layer using radar dual-polarization spectral analysis. *Journal of Atmospheric and Oceanic Technology*, *25*(3), 482–497.

Stewart, R. E., Marwitz, J. D., Pace, J. C., & Carbone, R. E. (1984). Characteristics through the melting layer of stratiform clouds. *Journal of the Atmospheric Sciences*, *41*(22), 3227–3237.

Stull, R. (2011). Wet-bulb temperature from relative humidity and air temperature. *Journal of Applied Meteorology and Climatology*, *50*(11), 2267–2269.

Szeto, K. K., Lin, C. A., & Stewart, R. E. (1988). Mesoscale circulations forced by melting snow. Part I: Basic simulations and dynamics. *Journal of the Atmospheric Sciences*, *45*(11), 1629–1641.

Trömel, S., Ryzhkov, A. V., Hickman, B., Mühlbauer, K., & Simmer, C. (2019). Polarimetric radar variables in the layers of melting and dendritic growth at X band: Implications for a nowcasting strategy in stratiform rain. *Journal of Applied Meteorology and Climatology*, *58*(11), 2497–2522.

Tyynelä, J., Leinonen, J., Moisseev, D., & Nousiainen, T. (2011). Radar backscattering from snowflakes: Comparison of fractal, aggregate, and soft spheroid models. *Journal of Atmospheric and Oceanic Technology*, *28*(11), 1365–1372.

Tyynelä, J., Leinonen, J., Moisseev, D., Nousiainen, T., & von Lerber, A. (2014). Modeling radar backscattering from melting snowflakes using spheroids with nonuniform distribution of water. *Journal of Quantitative Spectroscopy and Radiative Transfer*, *133*, 504–519.

Verlinde, J., Rambukkange, M. P., Clothiaux, E. E., McFarquhar, G. M., & Eloranta, E. W. (2013). Arctic multilayered, mixed-phase cloud processes revealed in millimeter-wave cloud radar Doppler spectra. *Journal of Geophysical Research: Atmospheres*, *118*, 13–199. https://doi.org/10.1002/2013JD020183

von Lerber, A., Moisseev, D., Leinonen, J., Koistinen, J., & Hallikainen, M. T. (2014). Modeling radar attenuation by a low melting layer with optimized model parameters at C-band. *IEEE Transactions on Geoscience and Remote Sensing*, *53*(2), 724–737.

Wolde, M., & Vali, G. (2001). Polarimetric signatures from ice crystals observed at 95 GHz in winter clouds. Part I: Dependence on crystal form. *Journal of the Atmospheric Sciences*, *58*(8), 828–841.

Wolfensberger, D., Scipion, D., & Berne, A. (2016). Detection and characterization of the melting layer based on polarimetric radar scans. *Quarterly Journal of the Royal Meteorological Society*, *142*, 108–124.

Yang, J., Lei, H., Hu, Z., & Hou, T. (2014). Particle size spectra and possible mechanisms of high ice concentration in nimbostratus over hebei province, china. *Atmospheric Research*, *142*, 79–90.

Zawadzki, I., Fabry, F., & Szyrmer, W. (2001). Observations of supercooled water and secondary ice generation by a vertically pointing X-band Doppler radar. *Atmospheric Research*, *59*, 343–359.

Zawadzki, I., Szyrmer, W., Bell, C., & Fabry, F. (2005). Modeling of the melting layer. Part III: The density effect. *Journal of the Atmospheric Sciences*, *62*(10), 3705–3723.

Zrnic, D. S., Balakrishnan, N., Ziegler, C. L., Bringi, V. N., Aydin, K., & Matejka, T. (1993). Polarimetric signatures in the stratiform region of a mesoscale convective system. *Journal of Applied Meteorology*, *32*(4), 678–693.